



Relationship between element-level and contact-level parameters of micromechanical and upscaled plasticity models for granular soils

Yang Liu¹ · C. S. Chang²

Received: 17 April 2018 / Accepted: 18 November 2019 / Published online: 1 January 2020
© Springer-Verlag GmbH Germany, part of Springer Nature 2020

Abstract

The models for stress–strain behavior of granular soils can be generally categorized into two approaches: the conventional plasticity approach and the micromechanics-based approach. In this work, we upscale a micromechanical model to a commonly used isotropic hardening plasticity model by assuming the “same” constitutive laws at different scales. The mathematically derived relationships between element-level and contact-level parameters are presented based on the condition that the two models would predict the same mechanical response, and a parameter calibration procedure is proposed. A comparative study is then conducted to investigate the differences of the predicted element behaviors arisen from the two models.

Keywords Constitutive model · Granular soils · Micromechanics · Multi-scale

1 Introduction

The modeling methodology for stress–strain behavior of granular soils can be generally categorized into two approaches: the conventional plasticity approach and the micromechanics-based approach. In the conventional approach, the material is treated as a continuum. The stress–strain behavior of the continuum material is defined for a “material point,” which represents an “infinitesimal volume element” of the continuum material. However, in the micromechanics-based approach, the stress–strain behavior is defined for a “representative volume element (RVE)” of finite size; some significant underlying mechanisms that occur at scales smaller than the representative volume element (RVE) can be considered.

A number of “micromechanics-based” approaches have been developed, which can be broadly classified into two categories: (a) discrete element method (DEM) and (b) granular mechanics. In the DEM approach, the stress–

strain behavior of the material is analyzed as a boundary value problem (e.g., [8, 38, 42]). The DEM approach does not give an explicit stress–strain relationship. In the granular mechanics approach, the stress–strain behavior of the representative volume element is derived explicitly based on the inter-particle behavior through an integration process.

Many granular micromechanics-based approaches have been proposed to construct elastic and elasto-plastic constitutive models. Elastic stress–strain models can be found in the earlier works of Rothenburg and Selvadurai [40], Walton [45], Jenkins [18], Chang [2], Chang et al. [5], Cambou et al. [1], Liao et al. [26], Krut and Rothenburg [23] and recently by Tran et al. [44], Krut [22] and Misra and Poorsolhjouy [31]. Elasto-plastic stress–strain models can be found in the works by Matsuoka and Takeda [30], Jenkins and Strack [19], Chang and Hicher [4], Nicot and Darve [36, 37], Maleej et al. [28], Misra and Yang [34], Zhu et al. [50] and more recently by Irani et al. [15], Xiong et al. [48].

The differences between the conventional plasticity approach and the micromechanics-based approach stem from their inherent nature. Model parameters and calibration procedures are basic issues in modeling stress–strain behavior for either micromechanical model or conventional plasticity model. In the conventional continuum approach,

✉ Yang Liu
yangliu@ustb.edu.cn

¹ Department of Civil Engineering, University of Science and Technology, Beijing 100083, China

² Department of Civil and Environmental Engineering, University of Massachusetts, Amherst, MA 01003, USA

the parameters describe directly the behavior of a particle assembly element (macro-scale), most of which can be obtained from experiments in laboratory such as triaxial compression or shear test, whereas in the micromechanics-based approach, the parameters describe the behavior of an inter-particle contact (micro-scale), which are difficult or even impossible to be obtained in laboratory directly. Thus, it is desirable to have an explicit relationship between the element-level parameters and the contact-level parameters. The relationship can be derived from a mathematical process, which ensembles the behavior of inter-particle contacts to obtain the stress–strain behavior of the particle assembly element.

Through this relationship, some contact-level parameters can be determined from element-level experiments in laboratory. For example, we can derive the relationship between inter-particle contact stiffness ratio and the Poisson's ratio of a particle assembly, even the specific values of normal and shear contact stiffness are unknown (see Sect. 2).

It is relatively easy to derive such relationship for linear elastic parameters. For nonlinear elastic materials, the relationship would be dependent on which nonlinear law is used. If the same form of nonlinear law is applied to both element level and contact level, a unique relationship can be obtained. Several relationships have been proposed for linear and nonlinear elastic parameters, for example, the moduli of a particle assembly can be predicted directly from the contact properties of the constituent particles in both isotropic and anisotropic stress conditions. (See the work by Chang et al. [5], Ng and Petrakis [35], Hicher and Chang [13].) These relationships provide a better understanding of the pressure-sensitive elastic behavior of granular media.

On the other hand, limited work has been done about the explicit relationships between contact-level parameters and element-level parameters for plasticity models (see [32, 33]). The main difficulty lies in the complex behavior of inter-particle contact stiffness, which has a strong dependency of contact force. Thus, anisotropic behavior of a particle assembly is induced by deviatoric stress, which causes the variation of contact force in various orientations. Another reason is the evolution of anisotropic fabric with the development of plastic deformation. It has been shown that during loading, the directions of contact planes between grains gradually change and their normal vectors rotate toward the major principal stress direction. This fabric change can also induce a significant anisotropy of materials, which cannot be included in conventional plasticity constitutive models (see [14, 39]).

The purpose of this work is to propose a relationship between the element-level parameters and the contact-level parameters for plasticity materials. However, it should be

noted that this relationship exists only under some specific conditions. For example, in case of the stress-dependent elastic material, upon loading, Young's modulus increases at element level, while inter-particle stiffness increases at particle level. Under isotropic compression, both the micromechanical model and continuum plasticity model behave as isotropic medium. When deviatoric stress is applied, the continuum model still behaves as isotropic medium; however, the micromechanical model would behave as an anisotropic model because the contact forces vary in each orientation. In other words, the relationship between the element-level parameters and the contact-level parameters exists only when the element is isotropically loaded. In a triaxial test, the relationship exists only at the very beginning of loading where the element is isotropically consolidated. With the development of strain during deviatoric loading, a unique relationship may not exist due to the difference in modeling methodology. Nevertheless, we can definitely obtain this relationship by taking the advantage that they behave same under the isotropic stress condition. It is also of interest to investigate the different performances between the conventional plasticity approach and the micromechanics-based approach under the deviatoric loading conditions.

Such studies are usually conducted through selecting two constitutive models (for example, a micromechanical model and a conventional plasticity model) or two numerical methods (for example, finite element method and discrete element method). As we know, the micromechanical model is more complex than the conventional plasticity model. The added complexity improves the performance of the micromechanical model. To assess the trade-off between simplicity and accuracy of the model, it is of interest to know the differences in modeling performance caused by the two different modeling methodologies (or approaches). However, very little research work had been carried out along this line, because it is not an easy task to separate the difference caused solely by the effect of the two different methodologies. In fact, the difference in model performance is caused by a number of factors other than the methodologies, such as the physical laws used in models or even the parameters used in simulations. Thus, in order to have a meaningful comparison for the difference caused solely by the effect of the two different methodologies, the following two factors must be considered:

(1) Models to be selected (a continuous plasticity model and a micromechanical model) must be constructed using the “same” constitutive laws, such as yielding condition, dilation pattern and hardening rule, etc. Here, the “same” means that the constitutive laws used in two models hold the same mathematical forms and physical mechanism, which are defined at different scale levels. For example, the

Coulomb friction law defined for an inter-particle contact plane with variables of normal and shear forces in a micromechanics-based model is considered the “same” as that for a material point defined with variables of normal and shear stresses in a continuous constitutive model.

This “same law” condition is required in order to make sure that the predicted differences of the macro-behaviors from these two models are caused from the method of analysis, rather than from the different constitutive laws.

(2) The models to be selected, each using its own set of parameters, must be calibrated from the same selected mechanical response measured from experiments, for example, the compressibility measured from an isotropic loading test, or the initial shear deformation measured from a shear load test. In other words, the two sets of parameters should be “equivalent” so that the two models predict the exact same macro-response for a specified set of stress conditions.

This condition is required so that the predicted differences of the macro-responses from these two models for general stress conditions (as the load progress) are not caused from the difference in arbitrarily selected parameters.

However, there is no existing pair of models available for this kind of analysis. So, we select a micromechanical model [4] and then upscale it to a conventional isotropic hardening plasticity model. We apply the same form of the yield function, the flow rule and the hardening law to both element level and contact level and investigate the relationships between the two sets of parameters and the specific performance differences of these two models.

The proposed upscaled model is very similar to the commonly used plasticity model such as nor-sand [17, 47] or the two-surface plasticity [29]. So, the relationship established below and the upscaled procedures are not only valid for the model proposed here, but also valid for the other commonly used isotropic hardening plastic models.

In the following, we will first discuss the relationship between the element-level parameters and the contact-level parameters for the elasticity case. Then, for the plasticity case, the specific yield function, the flow rule and the hardening law, and their associated parameters will be described for both the element level and the contact level. A relationship between the two sets of parameters will then be mathematically derived. Then, a comparative study is conducted to investigate the differences of the predicted element behaviors, such as stress–strain, dilating properties, etc., arisen from these two models. Such a comparative study may contribute to the assessment of the two modeling approaches: continuous approach and micromechanics-based approach.

2 Link between elastic properties at element level and contact level

2.1 Element level

The stress–strain relationship for the element level is

$$\dot{\sigma}_{ij} = C_{ijkl}\dot{u}_{k,l} \tag{1}$$

For elastic materials, the C_{ijkl} can be expressed in terms of Young’s modulus E and Poisson’s ratio ν as follows:

$$C_{ijkl} = \lambda g_{ij}g_{kl} + \mu(g_{ik}g_{jl} + g_{il}g_{jk}) \tag{2}$$

where λ and μ are Lamé constants, $\lambda = \nu E / (1 + \nu)(1 - 2\nu)$, $\mu = G = E / 2(1 + \nu)$, $g_{ij} = (\mathbf{e}_i, \mathbf{e}_j)$, and G is shear modulus.

For granular materials, the modulus is stress dependent; thus, Young’s modulus E (or bulk modulus $B = E / 3(1 - 2\nu)$) is considered to be dependent on mean stress σ_m , expressed as follows:

$$E = E_0 \left(\frac{\sigma_m}{p_{ref}} \right)^n \quad \text{or} \quad B = B_0 \left(\frac{\sigma_m}{p_{ref}} \right)^n \tag{3}$$

where $E_0 = 3(1 - 2\nu)B_0$, B_0 and n are two material constants: B_0 is the reference bulk modulus, and n is a constant exponent. The constant $E_0 = 3(1 - 2\nu)B_0$, and the reference pressure p_{ref} is taken to be 1 atm. The Poisson’s ratio ν is a constant.

2.2 Contact level

At the inter-particle contact level, an auxiliary local coordinate is established on each contact plane between two particles as shown in Fig. 1. The orientation of the contact plane is defined by the vector \mathbf{n} perpendicular to this plane.

On each contact plane, the contact stiffness includes normal stiffness, k_n^z , and shear stiffness, k_s^z . The elastic contact law is defined by the force and displacement relationship,

$$\dot{f}_i^z = k_{ij}^z \dot{\delta}_j^z \tag{4}$$

$$k_{ij}^z = k_n^z n_i^z n_j^z + k_r^z (s_i^z s_j^z + t_i^z t_j^z) \tag{5}$$

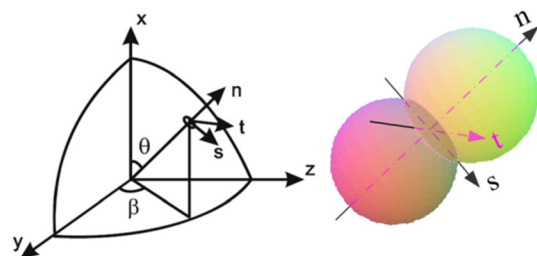


Fig. 1 Local coordinate system at an inter-particle contact

where f_i^α is an increment of force on the contact plane and k_{ij}^α is the elastic stiffness tensor, δ_j^α is the relative displacement between two contact particles; superscript α represents that the particle contact is in α orientation; n, s, t are three orthogonal unit vectors that form the local coordinate system in Fig. 1.

For a nonlinear elastic case, at the contact level, the elastic stiffness between two particles (normal k_n^α and tangential k_r^α) is assumed force dependent, following a revised Hertz-Mindlin’s formulation [5]:

$$k_n^\alpha = k_{n0}^\alpha \left(\frac{f_n^\alpha}{G_g l^2} \right)^n; \quad k_r^\alpha = \zeta^\alpha k_n^\alpha \tag{6}$$

where $k_{n0}^\alpha, \zeta^\alpha$ and n are three material constants in which k_{n0}^α is the reference normal contact stiffness, ζ^α is the ratio of shear stiffness to normal stiffness, and n is a constant exponent. f_n^α is the normal contact force between two particles, and G_g is the elastic modulus for the two particles. l is the branch length for the two particles. The elastic parameters for the micromechanical model include: the inter-particle elastic constants $k_{n0}^\alpha, \zeta^\alpha$ and n .

2.3 Link between parameters of element level and contact level

The relationship between the element-level and contact-level stiffness tensor can be established by using a static hypothesis or a kinematic hypothesis [3]. Here, we limit our discussion to the static hypothesis. The relationship is given by

$$C_{ijmp} = A_{ik}^{-1} A_{mn}^{-1} V \sum_{\alpha=1}^N k_{jp}^\alpha l_k^\alpha l_n^\alpha \tag{7}$$

where N is the total number of inter-particle contacts in the representative volume V . The branch vector l_k^α (l_n^α) is the vector joining the centers of two contact particles, and A_{ik} is a fabric tensor, defined as,

$$A_{ik} = \sum_{\alpha=1}^N l_i^\alpha l_k^\alpha \tag{8}$$

The summation in Eq. (7) can be expressed in an integral form:

$$\sum_{\alpha=1}^{N_c} k_{jp}^\alpha l_k^\alpha l_n^\alpha = \frac{N l^2}{2\pi} \int_0^{2\pi} \int_0^{\pi/2} k_{jp}(\beta, \theta) n_k(\beta, \theta) n_n(\beta, \theta) \zeta(\beta, \theta) \sin \theta d\theta d\beta \tag{9}$$

where l is the mean branch length; the distribution function $\zeta(\beta, \theta)$ is a probability density function, defined by:

$$\int_0^{2\pi} \int_0^{\pi/2} \zeta(\beta, \theta) \sin \theta d\theta d\beta = 1 \tag{10}$$

In integration form, A_{ik} can be expressed as:

$$A_{ik} = \frac{N l^2}{2\pi} \int_0^{2\pi} \int_0^{\pi/2} n_k(\beta, \theta) n_n(\beta, \theta) \zeta(\beta, \theta) \sin \theta d\theta d\beta \tag{11}$$

For isotropic packing structures,

$$\zeta(\theta, \beta) = \frac{1}{2\pi} \tag{12}$$

And for a linear isotropic elastic case, all contacts have the same stiffness (i.e., $k_{jp}(\beta, \theta) = \text{constant}$). After integration of Eq. (7) and compared with Eq. (2), the values of Young’s modulus and Poisson’s ratio can be derived as,

$$E = \frac{5N l^2 k_n^\alpha}{3V} \left(\frac{2 + 3\zeta^\alpha}{4 + \zeta^\alpha} \right); \nu = \frac{1 - \zeta^\alpha}{2 + 3\zeta^\alpha} \tag{13}$$

where $\zeta^\alpha = k_r^\alpha / k_n^\alpha$. Thus, the element-level parameters E and ν can be linked to the particle-level parameters k_n^α, k_r^α and the assembly packing information, N/V and branch length l (or particle size).

For a stress-dependent isotropic elastic case (see Eq. (3)), the element-level parameters B_0, ν and n can be expressed in terms of particle-level parameters $k_{n0}^\alpha, \zeta^\alpha$ and n [see Eq. (6)] as follows:

$$B_0 = \frac{4}{9} \left(\frac{N}{V} \right) r^2 k_{n0}^\alpha \tag{14}$$

where N is contact number in the representative volume V , and r is the radius of particles.

The Poisson’s ratio is the same as that given in Eq. (13) or

$$\zeta^\alpha = \frac{1 - 2\nu}{1 + 3\nu} \tag{15}$$

Both the elastic constant n , as shown in Eqs. (3) and (6), have the same value for both models (see [3]).

It is noted that these relationships exist only for the case of isotropic loading. In the micromechanical model, the contact force distribution evolves with the applied deviatoric stress. Thus, it is obvious that the assembly element is no longer an isotropic material, if the contact stiffness is force dependent.

3 Link between plasticity properties at element level and contact level

In order to find the element-level and contact-level parameters relationship, a simple plasticity model was upscaled from the micromechanical model. The model

belongs to one kind of commonly used isotropic hardening plastic model proposed by other researchers (such as [17, 29, 47]). So, the method used here is also valid for other isotropic plasticity models. As we know, the micromechanical model is a kinematic hardening model and the upscaled model proposed here is an isotropic hardening model. However, the explicit relationship between element-level and contact-level parameters can be obtained under the isotropic compression stress state (or the initial state of shearing).

3.1 Element level

The yield function is chosen to be of Coulomb type, the flow rule is based on the shear dilatancy equation of Taylor type, and the isotropic hardening rule is chosen to be of hyperbolic type given as follows,

Yield function

$$f(p, q_r, \kappa) = q - p\kappa(\varepsilon_r^p) = 0 \quad (16)$$

Flow rule

$$\frac{\dot{\varepsilon}_v^p}{\dot{\varepsilon}_r^p} = D \left(M - \frac{q}{p} \right) \quad (17)$$

Hardening rule

$$\kappa(\varepsilon_r^p) = \frac{G^p M_p \varepsilon_r^p}{p M_p + G^p \varepsilon_r^p} \quad (18)$$

where p is the mean stress, $p = (\sigma_1 + \sigma_2 + \sigma_3)/3$; q is the shear stress ($q = \sqrt{3J_2}$, where J_2 is the second invariant of deviator stress tensor); ε_r^p and ε_v^p are plastic shear and volumetric strain; M is the slope of critical state line in $p - q$ space, $M = 6 \sin \phi_{cs}/(3 - \sin \phi_{cs})$. D is the dilatancy parameter, $M_p = 6 \sin \phi_p/(3 - \sin \phi_p)$, and the value of ϕ_p is made to be a function of density state as shown in Eq. (19):

$$\tan \phi_p = \left(\frac{e_{cr}}{e} \right)^m \cdot \tan \phi_{cs} \quad (19)$$

where m is a positive number that is dependent on the type of soil (especially particle shape). For dense packing, the frictional angle ϕ_p is greater than the critical state friction angle (ϕ_{cs}). After peak load, the packing structure dilates, the increase in void ratio is associated with a reduction of frictional angle ϕ_p , and this results in a strain-softening phenomenon.

The relationship between critical state void ratio (e_{cr}) and mean effective stress from the following equation is called critical state line (CSL), given by:

$$e_{cr} = e_{ref} - \lambda \left(\frac{p'}{p_{ref}} \right)^\xi \quad (20)$$

where p' is the effective mean stress and p_{ref} is the reference pressure, which is taken to be 1 atm. Three parameters are required to define the critical state line (CSL): e_{ref} (zero intercept), λ (CSL slope) and ξ (CSL curvature).

The plastic stiffness G^p is assumed to be related to the bulk elastic stiffness B by a constant χ , given by

$$G^p = \chi B = \chi B_0 \left(\frac{p}{p_{ref}} \right)^n \quad (21)$$

The initial slope of the hyperbolic curve (Eq. 18) is G^p/p , and the value of $\kappa(\varepsilon_r^p)$ asymptotically approaches M_p . One can see that the flow rule is nonassociative.

Comparing with the three commonly used isotropic hardening models (such as [17, 29, 47]), the proposed model has similar characteristics in the following aspects:

(1) Critical state and state parameters

All models including this model proposed here are built in the framework of CCSM (critical state soil mechanics). Similar state parameters are used to define the peak and dilatancy stress ratios of sand. All these models are capable of simulating stress–strain behavior of sands under monotonic, drained and undrained loading conditions.

(2) Yielding equation

Although the shape of yielding surface proposed here is different from wood's model and nor-sand model, yielding function in these three models are of Coulomb type, i.e., the materials yield when q/p reaches a certain value. The yield surface in the two-surface plasticity model appears as a simple Misses-type circle in deviatoric stress ratio space and as a moving circular cone in general space.

(3) Dilatancy equation (or flow rule)

The dilatancy equation (Eq. 17) has the same form as nor-sand model [17], Wood's model [47] and the two-surface plasticity model [29], i.e., $\delta\varepsilon_p/\delta\varepsilon_q = C(M_c - \eta)$, where C is a material constant. If $C = 1$, the dilatancy equation has the same form as Cam-clay model.

(4) Hardening rule

The hardening rule proposed here (Eq. 18) is very similar to wood's model in form. The hardening function in nor-sand is a proportional function of the maximum hardness controlled by state parameters ψ . In the two-surface plasticity model, the isotropic hardening is plasticity volumetric strain hardening, while the bounding surface controls the kinematic hardening of the yield surface.

As described above, the model proposed here is an isotropic hardening model, built within the framework of CCSM.

3.2 Contact level

The same forms of yield surface, flow rule, and hardening rule are applied to the inter-particle contact behaviors (see [4]).

$$\text{Yield function } F(f_n^z, f_r^z, \kappa) = f_r^z - f_n^z \kappa(\delta_r^p) = 0 \quad (22)$$

$$\text{Flow rule } \frac{\dot{\delta}_n^p}{\dot{\delta}_r^p} = d \left(\tan \phi_0 - \frac{f_r^z}{f_n^z} \right) \quad (23)$$

$$\text{Hardening rule } \kappa(\delta_r^p) = \frac{k_{r0}^p \tan \phi_p \delta_r^p}{f_n^z \tan \phi_p + k_{r0}^p \delta_r^p} \quad (24)$$

In these equations, the resultant shear force f_r^z and the resultant plastic sliding δ_r^p can be defined as:

$$f_r^z = \sqrt{(f_s^z)^2 + (f_t^z)^2} \text{ and } \delta_r^p = \sqrt{(\delta_s^p)^2 + (\delta_t^p)^2} \quad (25)$$

The yield function is assumed to be of Mohr–Coulomb type. The direction of plastic sliding at an inter-particle contact is governed by the flow rule, where d is a material constant that controls the intensity of dilation and is typically equal to 1.0. ϕ_0 is a material constant which, in most cases, can be considered equal to the reference apparent internal friction angle ϕ_μ , which, in value, is very close to the internal friction angle ϕ_{cs} , measured at critical state. Similar to the critical state void ratio, the reference apparent inter-particle friction angle (ϕ_μ) is an intrinsic material property for a given type of soil. $\tan \phi_0$ represents the obliquity at which the dilation is zero. The angle of ϕ_0 is corresponding to the concept of “phase transformation” as defined by Ishihara [16] or “characteristic state” as defined by Luong [27].

The sliding direction represented by Eq. 23 is not perpendicular to the yield surface. Thus, the flow rule is also nonassociative. The hardening function $\kappa(\delta_r^p)$ is defined by a hyperbolic curve in $\kappa - \delta_r^p$ plane, which involves two material parameters, ϕ_p and k_{r0}^p .

The plastic stiffness k_{r0}^p is assumed to relate to the elastic stiffness k_n^z by a constant ζ^p :

$$k_{r0}^p = \zeta^p k_n^z = \zeta^p k_{n0}^z \left(\frac{f_n^z}{G_s l^2} \right)^n \quad (26)$$

The initial slope of the hyperbolic curve is k_{r0}^p/f_n^z , and the value of $\kappa(\delta_r^p)$ asymptotically approaches the apparent inter-particle friction angle (i.e., $\tan \phi_p$). For the purpose of compensating the errors due to the assumptions used in the static hypothesis for the relationships between contact forces and element stresses, the value of ϕ_p is made to be a function of density state as previously shown in Eq. (19).

3.3 Link between parameters of element level and contact level

The element-level plastic constants are χ , D , m , and the inter-particle plastic constants are ζ^p , d , m . Critical state constants, e_{ref} , λ , ξ and ϕ_{cs} are used in both element-level and contact-level models. The values for the four critical state parameters, namely e_{ref} (zero intercept), λ (CSL slope), ξ (CSL curvature) and ϕ_{cs} (CSL friction angle), are the same in both models for a given soil.

We aim to find the relationships between these parameters through an integration process over all inter-particle contacts in the assembly. As mentioned previously, under a general loading condition, inter-particle contact forces vary for each contact, and the assembly element becomes anisotropic. Thus, the material can no longer be regarded as an isotropic hardening plasticity model.

The two parameters in flow rule: d for the micromechanical model and D for the plasticity model can be determined from the measured initial dilation at the beginning of shear after isotropic consolidation. By using Eq. (54) shown in “Appendix 1,” the ratio of macro-scale plastic volumetric strain increment and plastic shear strain increment can be derived by integrating Eq. (23) over all contact orientations. At the beginning of shear after the specimen is isotropically stressed ($q = 0$), the ratio can be expressed as follows (see “Appendix 1” for derivation),

$$\left(\frac{\dot{\epsilon}_v^p}{\dot{\epsilon}_r^p} \right)_0 = \frac{15d \tan \phi_{cs}}{d \tan \phi_{cs} + 6} \quad (27)$$

For the plasticity model, the ratio of plastic volumetric strain increment and shear strain increment can be obtained according to Eq. (17) as follows,

$$\left(\frac{\dot{\epsilon}_v^p}{\dot{\epsilon}_r^p} \right)_0 = DM \quad (28)$$

By equating Eqs. (27 and 28), we obtain the relationship of d and D as follows,

$$d = \frac{6DM}{\tan \phi_{cs}(15 - DM)} \quad (29)$$

The two parameters ζ^p and χ , in connection to hardening rule, can be determined from the measured initial plastic stiffness at the beginning of shear after isotropic consolidation. For the micromechanical model, we obtain the initial plastic shear strain increment by integrating the contact deformation in all orientations (see Eqs. 54–57 in “Appendix 1”), as follows,

$$\dot{\epsilon}_r^p = \frac{1}{3B\zeta^p} \left(\frac{1}{15} d \tan \phi_{cs} + \frac{2}{5} \right) \dot{q} \quad (30)$$

For the conventional plasticity model, the plastic shear strain increment at the beginning of shear is,

Table 1 Summary of required parameters for both models

Model	critical state			Inter-particle contact / assembly						
				elastic		plastic				
Micromechanical Model	e_{ref}	λ	ξ	n	K_{n0}^α	ζ^α	ζ^p	d	m	ϕ_{cs}
Plasticity Model				B_0	ν	χ	D			

$$\dot{\epsilon}_r^p = \frac{\dot{q}}{G^p} \tag{31}$$

Equating Eqs. (30)–(31) and using Eq. (21), we obtain the relationship of ζ^p and χ as follows,

$$\zeta^p = \frac{d \tan \phi_{cs} + 6}{45} \chi \tag{32}$$

The values of plastic constant m are the same for the plasticity and the micromechanical models, because ϕ_p is defined by the same evolution law as shown in Eq. (19).

The parameters of conventional plasticity model and micromechanical model are summarized in Table 1. All parameters can be determined from the stress–strain curves obtained from compression triaxial tests (see Sect. 4).

3.4 Macro-stress–strain relationship and computation scheme

Based on the classical plastic theory, the stress–strain relationship of the upscaled plasticity model can be easily derived and the computation scheme follows the standard elastic–plastic integral scheme, which will be not repeated here.

With previously described elastic and plastic inter-particle behaviors, the incremental force–displacement relationship for two particles under sliding can be expressed as,

$$f_i^\alpha = k_{ij}^{ep} \dot{\delta}_j^\alpha \tag{33}$$

where k_{ij}^{ep} is the elastic–plastic stiffness tensor. The stress–strain relationship for a packing will then be obtained by integrating the behavior of inter-particle contacts in all orientations. Using the static hypothesis proposed by Liao et al. [26], we obtain the relation between the macro-strain and inter-particle displacement,

$$\dot{u}_{j,i} = A_{ik}^{-1} \sum_{\alpha=1}^N \dot{\delta}_j^\alpha l_k^\alpha \tag{34}$$

where the branch vector l_k^α is the vector joining the centers of two contact particles. For simple, N is defined as the total number of contact orientations. The variables $\dot{\delta}_j^\alpha$ and

l_k^α are defined, respectively, as the averaged values for all contacts belong to the α th orientation. A_{ik} is the fabric tensor, defined as in Eq. (10). Using the principle of energy balance, the mean force on the contact plane of each orientation is

$$f_j^\alpha = \dot{\sigma}_{ij} A_{ik}^{-1} l_k^\alpha V \tag{35}$$

where the stress increment $\dot{\sigma}_{ij}$ can be obtained by the contact forces and branch vectors for contacts using the equilibrium condition and divergence theorem as follows,

$$\dot{\sigma}_{ij} = \frac{1}{V} \sum_{\alpha=1}^N f_j^\alpha l_i^\alpha \tag{36}$$

The derived Cauchy stress expression in Eq. (36) from volume average principle leads to the results obtained by Christoffersen et al. [7] and Rothenberg and Selvadurai [40] derived from the principle of virtual work.

The final incremental stress–strain relations can be derived that includes both elastic and plastic behavior, given by

$$\dot{u}_{i,j} = C_{ijmp} \dot{\sigma}_{mp} \tag{37}$$

where $C_{ijmp} = A_{ik}^{-1} A_{mn}^{-1} V \sum_{\alpha=1}^N k_{jp}^\alpha l_k^\alpha l_n^\alpha$, as described in Eq. (7). The summation in Eq. (37) can be replaced by an integral over orientations. The integral can lead to a closed-form solution for the elastic modulus of randomly packed equal-size particles [6]. However, in the elastic plastic behavior, due to the nonlinearity nature of the local constitutive equation, a numerical calculation with iterative process is necessary to carry out the summation in Eq. (37). In order to facilitate the numerical calculation, the orientations are selected to coincide with the locations of Gauss integration points in a spherical coordinate. Summation over these orientations with the Gauss weighting factor for each orientation is equivalent to determining the integral over orientations. We found that the results were more accurate by using a set of fully symmetric integration points. From a study of the performance of using different numbers of orientations, we found $N \geq 74$ to be adequate.

For a strain-controlled test, Eq. (37) is not useful especially at the after peak range of strain softening. In this case, a method of “plastic predictor–plastic corrector” was adopted to obtain the solution. For a mix-mode loading condition, additional process of distributing the unbalance stresses was also needed. The detailed procedure is not included here.

4 Parameter determination of the two models

In this section, we propose a procedure to determine the element-level and contact-level parameters for both the conventional plasticity and the micromechanical models; both sets of parameters are calibrated from the same selected mechanical response measured from experiments. For convenience, the two selected mechanical responses are: (1) the compressibility measured from a drained isotropic compression loading test, and (2) the initial shear deformation measured from the beginning of a shear load test on an isotropically consolidated sample.

We take the Japanese silica sand test result [21] as an example to illustrate the procedure. First, the critical state parameters are determined. Then, the elastic parameters are determined from experimental test data, and at last the plastic parameters are determined.

4.1 Critical state parameters

Three critical state parameters, namely e_{ref} (intercept), λ (CSL slope) and ζ (CSL curvature), are required to define the critical state void ratio. To do so, drained or undrained triaxial tests are needed to attain the critical state line (CSL) [46]. By fitting Eq. (20) to the critical state data, the critical void ratio parameters e_{ref} , λ , and ζ are determined. Figure 2 shows CLS of silica sand [21], by fitting the CSL line, $e_{ref} = 0.66$ and $\lambda = 0.82$.

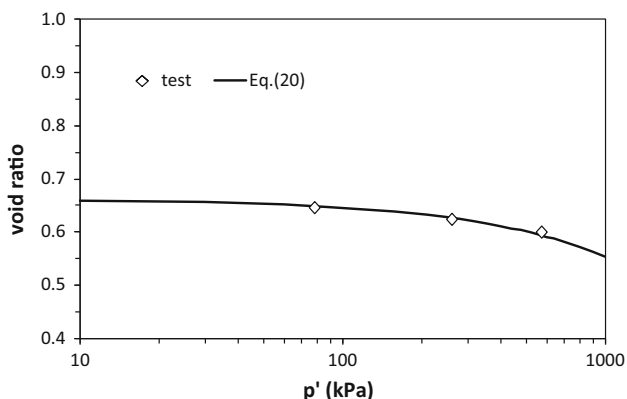


Fig. 2 Critical State lines for Japanese Silica Sand [21]

The critical state friction angle ϕ_{cs} (noting it is also the plastic parameter) can be obtained by measuring the slope of critical state line, M , in p' - q space. The following equation describes the relationship between critical state friction angle and M-line slope.

$$M = \frac{6 \sin \phi_{cs}}{3 - \sin \phi_{cs}} \tag{38}$$

For the silica sand [21] $\phi_{cs} = 30.96$, the corresponding M is 1.243.

4.2 Elastic parameters

The isotropic compression test is used to determine the elastic parameters B_0 and n of the conventional plasticity model. Figure 3 shows the isotropic compression line (ICL) of sand [21]. By fitting the ICL, parameters B_0 and n can be determined. For this sand, we obtain $B_0 = 6.53$ MPa and $n = 0.8$.

The elastic constant n for the micromechanical model is the same as the elastic constant n for the conventional plasticity model. The parameter k_{n0}^z for the micromechanical model can be calculated from Eq. (14) after B_0 is obtained, $k_{n0}^z = 9 \times B_0/4 = 14.7$. The parameters for both conventional plasticity and micromechanical models fit well the experimental curve.

Another elastic parameter for the conventional plasticity model is Poisson’s ratio ν , which can be estimated from the axial and volumetric strains measured in a triaxial compression test, as discussed by many researchers [11, 24]. The corresponding parameter ζ^z for the micromechanical model can be calculated with the relationship of ζ^z and ν using Eq. (15). For the silica sand [21], $\nu = 0.15$, and $\zeta^z = 0.48$.

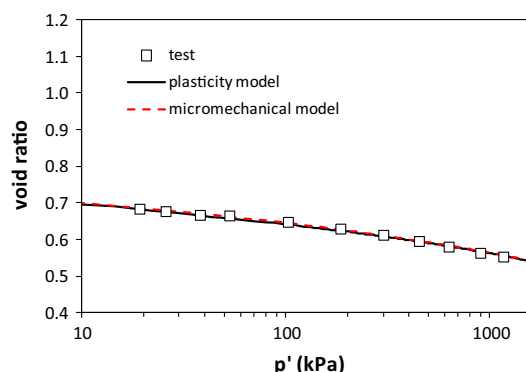


Fig. 3 Simulated and measured values of isotropic compression lines for silica sand tested by Konishi et al. [21]

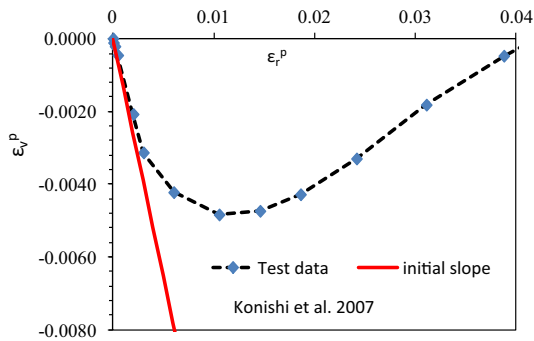


Fig. 4 Determination of parameter D

4.3 Plastic parameters

After the three elastic parameters B_0 , n and ν have been determined, elastic strains can be calculated using Eq. (1), and the plastic strain can then be obtained by subtracting the elastic part from the measured total strain.

Parameter D and d Parameter D can be obtained from the initial slope of the $\varepsilon_v^p \sim \varepsilon_r^p$ curve. Figure 4 is the $\varepsilon_v^p \sim \varepsilon_r^p$ curve for the sand sample under triaxial shear [21] with a confining pressure of 400 kPa. The measured initial slope of the curve, $\varepsilon_v^p/\varepsilon_r^p$, is -1.67, and then D can be determined

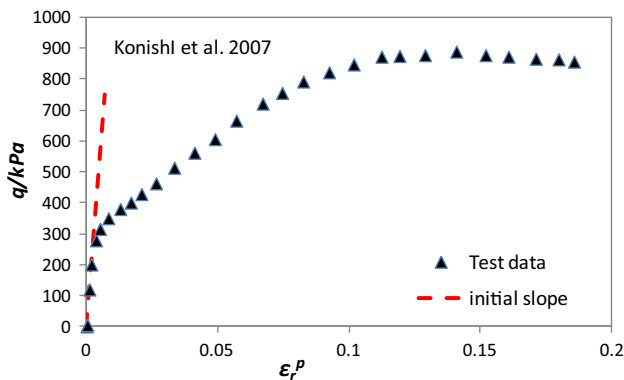


Fig. 5 Determination of parameter χ

by Eq. (28). Using $M = 1.243$, the value $D = 1.67/1.243 = 1.35$. In model prediction, the average value of $D = 1.2$ for different confining pressures can be used.

Parameter d of the micromechanical model can be obtained by the relationship of D and d using Eq. (29) after D is determined. For the silica sand [21], $d = 1.1$.

Parameter χ and ζ^p For the conventional plasticity model, the initial slope of $q - \varepsilon_r^p$ curve is G^p . The parameter χ by definition can be obtained by $\chi = G^p/B$, where the value of B is calculated by Eq. (3), i.e., $B = B_0(p/p_{ref})^n$.

For example, Fig. 5 is $\varepsilon_r^p \sim q$ curve of the undrained triaxial compression test for sands under confining pressure of 400 kPa [21], from which we obtain $G^p = 115 \text{ MPa}$, $B = 6.65 \times (400/101.35)^{0.8} = 19.58 \text{ MPa}$; then, the value of χ can be determined by $\chi = G^p/B = 5.87$.

Parameter ζ^p of the micromechanical model can be obtained from the relationship between χ and ζ^p in Eq. (32) after parameters d and χ have been determined. For the silica sand, the parameter $\zeta^p = 0.88$.

Parameter m Parameter m can be calculated from Eq. (19) involving four parameters: the friction angle at peak ϕ_p , the critical void ratio e_{cr} , the void ratio e at peak and the critical state friction angle ϕ_{cs} . Among the 4 parameters, e_{cr} and ϕ_{cs} are known critical state parameters. The values of void ratio e and the friction angle ϕ_p can be obtained from an undrained triaxial test.

For example, from the experimental data, we obtain $e = 0.66$, and $M_p = 1.60$ at peak stress state for the sand sample [21]. Using the critical state parameters, we obtain $e_{cr} = 0.6087$ and $\phi_{cs} = 30.96^\circ$, and then, we can calculate $m = 3.76$ using Eq. (19). The averaged value of $m = 4.0$ for different confining pressures was later used in model prediction.

Table 2 Parameters for both models used in the simulation of drained and undrained conditions

critical state			Inter-particle contact / assembly						
			elastic			plastic			
e_{ref}	λ	ξ	n	K_{n0}^α/B_0	ζ^e/ν	ζ^p/χ	D/d	m	ϕ_{cs}
0.66	0.016	0.8	0.8	14.18/6.3	0.286/0.25	1.132/8	0.6152/0.7	4	31

5 Comparison of two models based on the proposed parameters relationship

In the micromechanical modeling, the overall stress–strain behavior of the assembly is derived from integrating the inter-particle behavior over all contacts. The conventional modeling approach on the other hand does not account for the behavior at particle level. Thus, the differences between the two approaches are due to their inherent nature. In this section, we compare the selected two models based on the relationship between element-level and contact-level parameters, and the calibration procedure mentioned above.

5.1 General numerical results from two models

In this section, we compare the general performances and trends of the two models without comparing with the experimental results. We first choose a set of parameters for the conventional plasticity model, and then based on the relationship of Eqs. (14), (15), (29) and (32) the corresponding “equivalent” parameters for the micromechanical model are determined. All parameters are listed in Table 2.

Using these two models, the stress–strain curves for soil with three different densities are simulated under both drained and undrained conditions. The predicted stress–strain responses are used to study the predicted differences between the two models.

Figure 6a shows the simulated stress–strain and stress–path curves for tests under undrained conditions, and Fig. 6b shows the simulated stress–strain and the volumetric strain curves for tests under drained conditions.

At the beginning of shear loading after the sample is isotropically consolidated, both models predict the same response because the parameters are calibrated based on the stress conditions at the beginning of shear, and the sample is isotropic at this stage. As additional load is applied, the sample deviates from the isotropic condition and differences between the predicted responses are expected.

For the tests under undrained conditions, loose soil specimens show shear softening behavior (③, ④ in Fig. 6a). However, for the tests under drained conditions, dense soil specimens show shear softening behavior (①, ② in Fig. 6b). In these shear softening curves, the peak shear stresses predicted by the micromechanical model are

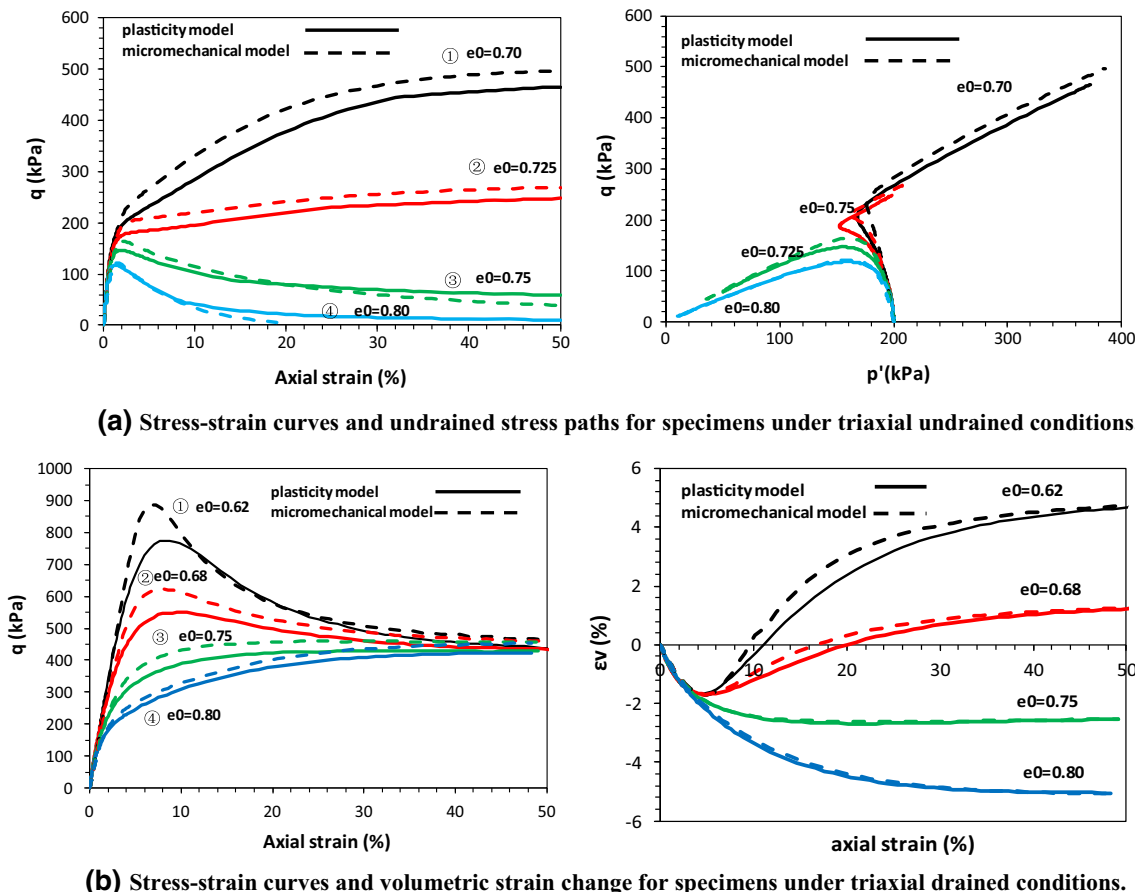


Fig. 6 Comparison of simulation results computed from both models

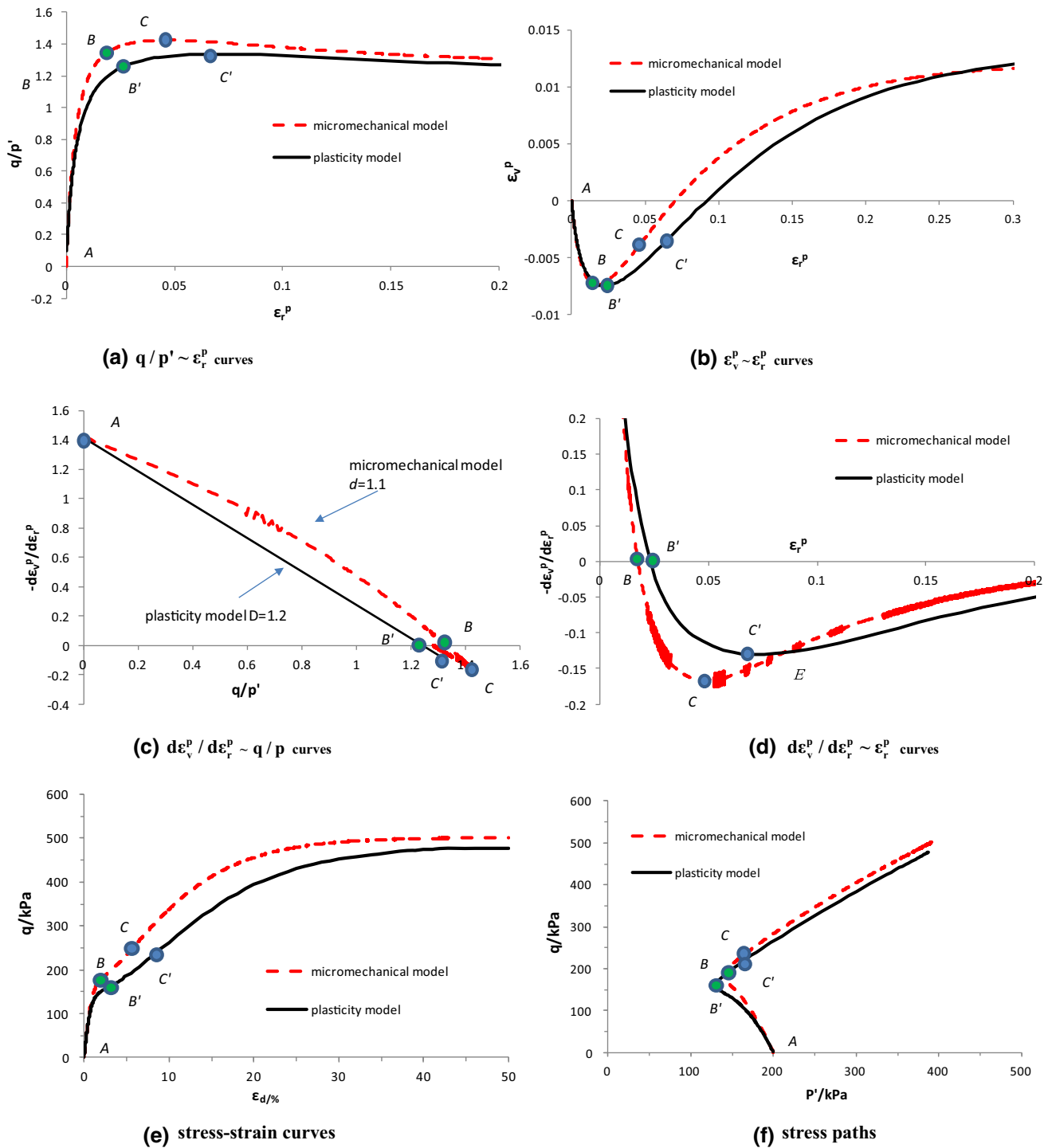


Fig. 7 Comparison of the stress–strain and dilatancy behavior simulated by the two models

higher and the axial strains needed to reach peak shear stresses are less than those predicted by the conventional plasticity model. On the other hand, the predictions show strain hardening behavior for dense soil specimens under undrained conditions (①, ② in Fig. 6a) and for loose soil specimens under drained conditions (③, ④ in Fig. 6b). For the strain hardening curves, the predicted strength by the

micromechanical model is higher than that predicted by the conventional plasticity model.

5.2 Dilatancy and induced anisotropy

In this section, we discuss the predicted behavior of dilatancy from both models. Figure 7 shows the simulation

results for an undrained triaxial test using the micromechanical model and the conventional plasticity model. The simulation results were obtained using the two sets of parameters shown in Table 2, except the values of d/D : in order to see more clearly the effect of dilatancy, we increase the value from $d = 0.615$ to 1.1 and the corresponding value of D from 0.7 to 1.2 (using Eq. 29).

Figure 7a shows the stress–strain curves on the $q/p' \sim \varepsilon_r^p$ plane, and Fig. 7b shows the plastic volumetric strain ε_v^p versus shear strain ε_r^p curve. In these plots, Point “A” is the point representing the beginning of shear loading after isotropic consolidation. Points “B” and “B'” are the phase transformation points (from contraction to dilation) (see Fig. 7b); points C and C' are the points at the peak stress ratios (see Fig. 7a) predicted from the two models.

The predicted dilatancy curves are plotted in Fig. 7c on the plane with plastic strain ratio increment ($d\varepsilon_v^p/d\varepsilon_r^p$) versus stress ratio (q/p) and in Fig. 7d on the plane with ($d\varepsilon_v^p/d\varepsilon_r^p$) versus plastic shear strain ε_r^p . The value of $d\varepsilon_v^p/d\varepsilon_r^p$ represents the dilation/contraction tendency at a given stresses or strain level.

One can see from the point “A” in Fig. 7c that the values of $d\varepsilon_v^p/d\varepsilon_r^p$ for both models at the beginning of shear load (or the initial slope of the curve in Fig. 7b) are the same. This is not a surprise because, at this point, the properties are same for all orientations. The values of d and D are related by Eq. 29. However, with the development of shear strain, the sample becomes anisotropic, and one can see from Fig. 7c that the dilatancy developments are very different for the two models. The essential difference is that the micromechanical model predicts a nonlinear curve in the plot of plastic strain ratio, $d\varepsilon_v^p/d\varepsilon_r^p$ versus stress ratio, q/p , whereas the conventional plasticity model gives a linear line. Numerical results indicate that this difference becomes significant for larger values of the dilatancy parameters (D and d).

For both Fig. 7c, d, the predicted maximum dilation tendency point (C or C') from the two models is corresponding to the reflecting point of $\varepsilon_v^p \sim \varepsilon_r^p$ curve in Fig. 7b, and to the point of peak stress ratio, as shown in Fig. 7a. One can also see that the maximum volume contraction point (B or B') in Fig. 7b is corresponding to the zero slope of the $\varepsilon_v^p \sim \varepsilon_r^p$ curve (or zero dilatancy point), which occurs when $q/p' = M$.

Comparing the dilatancy behavior of the two models, it is observed that, given a fixed value of stress ratio, q/p' in Fig. 7c, the micromechanical model gives a higher contraction tendency before the phase transformation and a lower dilation tendency after the phase transformation. However, it is noted that, given a fixed value of plastic shear strain, ε_r^p in Fig. 7d, the dilatancy behavior is completely opposite to the above statement: i.e., the

micromechanical model gives a “lower” contraction tendency before the phase transformation and a “higher” dilation tendency after the phase transformation.

The above statements are seemingly contradictory but actually consistent. This can be made clear by examining Fig. 7a; for a fixed value of shear strain, ε_r^p , there are two different corresponding stress ratios, q/p' of two models, and vice versa. Therefore, when comparing the levels of dilatancy of the two models, it should be referenced to the condition of given stress or strain level.

It is also interesting to compare the stress–strain curves (Fig. 7e) and undrained stress path (Fig. 7f) predicted from the two models. Obviously, the peak of stress ratio, q/p' (point C or C' in Fig. 7a), is not corresponding to the peak shear stress, q in Fig. 7e; the peak stress ratio is reached long before the peak value of the shear stress q is reached.

One can observe from Fig. 7f that at the initial portion of the shear loading, the stress paths predicted from both models show contraction behavior. Based on our previous conclusion from Fig. 7c, for a given stress level, the micromechanical model predicts higher contraction before the transformation point. Thus, the stress path predicted from the micromechanical model should be on the left side of the stress path predicted from the conventional plasticity model, which seems to contradict the results shown in Fig. 7f.

Therefore, there must be another mechanism in the micromechanical model, which can create dilatancy and offset the volume strain induced by plastic shear strain. This specific mechanism will be discussed below.

Under the condition of $d = D = 0$, Fig. 8 shows the predicted results for triaxial undrained loading conditions using both models. One can see that the stress path of the conventional plasticity model is a vertical line in p' - q space (constant p') (Fig. 8a). However, the stress path for the micromechanical model moves to the right side, indicating a negative pore pressure generation due to the dilatancy tendency. The negative pore pressure generation results in a higher strength which can be seen from Fig. 8b. This phenomenon mentioned here cannot be captured by the upscaled plasticity model, which can be explained from a micromechanics viewpoint as follows:

As mentioned previously, during deviatoric load, the stiffness becomes different for contact planes in various directions. This leads to a stress-induced elastic anisotropy of the material. It is well known that, for an anisotropic elastic material under a constant mean stress condition, applied shear stress can cause an increase in elastic volumetric strain, ε_v^e , in a drained triaxial experiment. Under an undrained condition, this tendency of volume strain increase causes a negative pore pressure generation, resulting in an increase in effective mean stress and shear

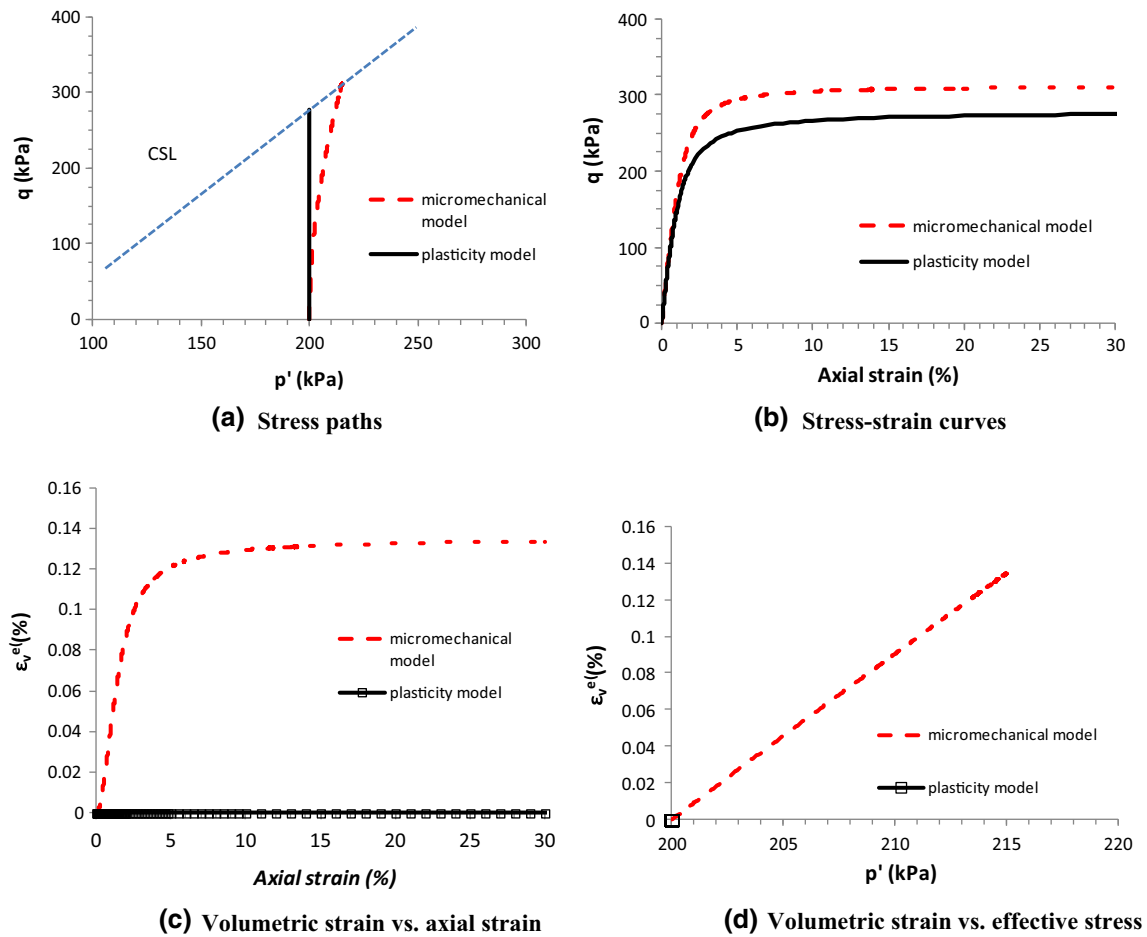


Fig. 8 Simulation results with the case of $d = D = 0$ for two models

strength as shown in Fig. 8a, b. The predicted elastic volumetric dilation due to axial strain is shown in Fig. 8c. The predicted elastic volumetric compression due to the increase in mean stress is shown in Fig. 8d. It is noted that in this undrained triaxial test, the sum of elastic compression and elastic dilation is zero. For the conventional plasticity model with dilatancy constant $D = 0$, one can see from Fig. 8c, d that there is no elastic dilation or compression under the applied shear load.

Thus, the shape of stress path predicted by the micromechanical model shown in Fig. 8a is caused as a result of the stress-induced elastic anisotropy. In the case of $d \neq D \neq 0$, the shape of stress path of the micromechanical model shown in Fig. 7f is affected not only by the plastic contraction but also by the elastic dilation.

5.3 On the aspect of inherent anisotropy

The anisotropy of the packing structure creates anisotropy of the mechanical behavior whose directions are identical

to those of the geometric anisotropy. The anisotropy of granular assembly can be featured by a fabric tensor,

$$F_{ij} = \int_0^{2\pi} \int_0^\pi \xi(\theta, \beta) n_i n_j \sin \theta \, d\theta \, d\beta \tag{39}$$

where $\xi(\theta, \beta)$ is distribution of inter-particle contact orientations, which can usually be expressed by a harmonic Fourier expansion in a spherical coordinate system.

One of the main interests of the micromechanical model is its capacity to take into account a structural anisotropy. In fact, in the micromechanical model, the decomposition of the constitutive equations along a set of planes allows formulating the dependency of the parameters with respect to the orientation. Therefore, inherent anisotropy can be easily incorporated to obtain the response of a material [4, 49].

The upscaled conventional plasticity model, used here for comparison, is an isotropic hardening model, which does not consider the factor of inherent material anisotropy.

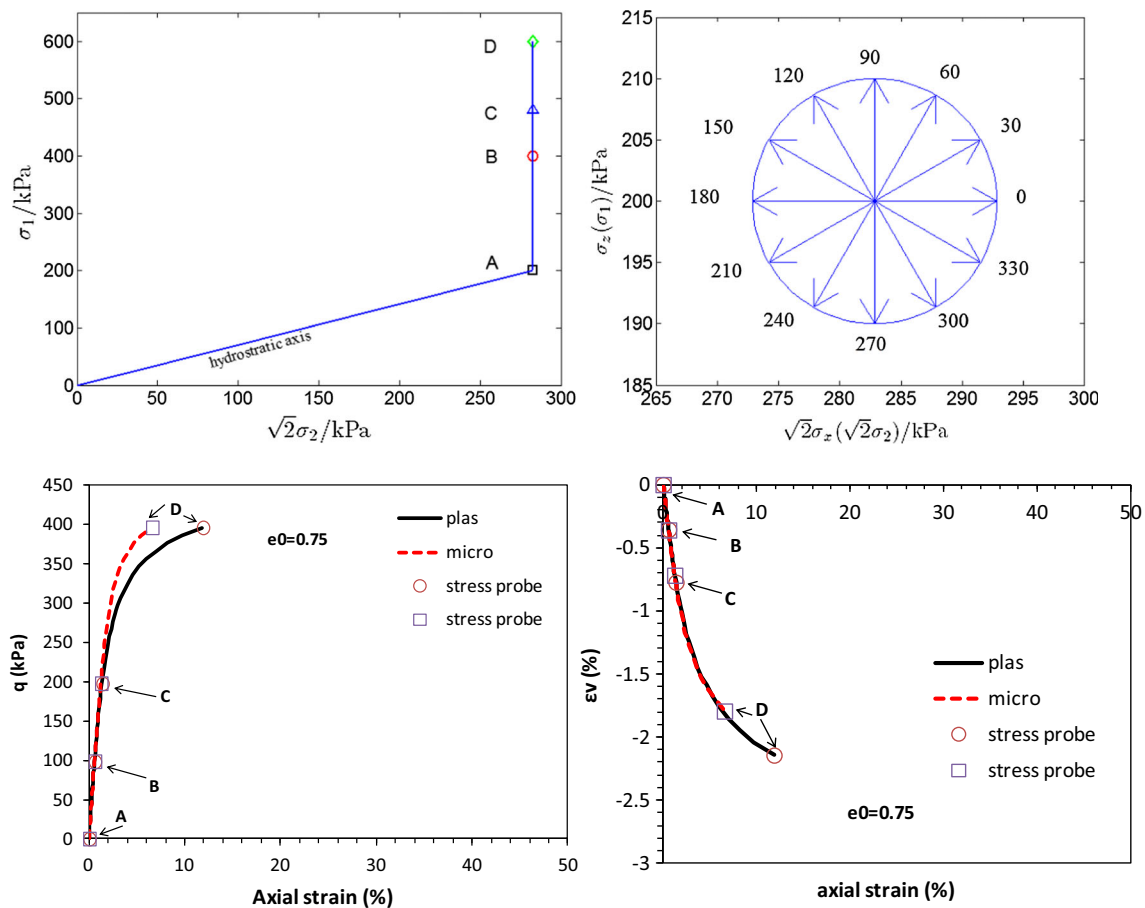


Fig. 9 Different stress state of stress probe and the location of stress point on stress–strain curve and axial–volumetric strain curve

5.4 Response envelopes predicted from both models

Response envelopes are a useful tool for validating and comparing constitutive equations [10, 20, 41, 43]. The original concept of response envelopes was presented by Lewin and Burland [25] and Gudehus [12] in context with the development of constitutive equations. In general, to obtain a response envelope, a soil element is subjected to a certain stress or strain increment. The corresponding “response” of the soil in the form of either strain or stress is determined and described graphically. The direction of the applied stress or strain increment with a constant absolute value is then varied and leads to different stress or strain responses, endpoints of which are connected to form response envelopes.

The strain response envelopes predicted from the upscaled plasticity model and from the micromechanical model were compared in the present work. After an initial isotropic compression with confining pressure 200 kPa, a drained triaxial loading test was simulated in axisymmetric conditions. Stress probe test is performed at 4 stress points, i.e., points A, B, C and D as shown in Fig. 9. Point A

($\sigma_1 = \sigma_2 = \sigma_3 = 200$ kPa, $\eta = q/p = 0$) is an initially isotropic stress state, and the other three points are initially anisotropic stress states (B: $\sigma_1 = 400$, $\sigma_3 = 200$ kPa, $\eta = 0.75$; and C: $\sigma_1 = 480$, $\sigma_3 = 200$ kPa, $\eta = 0.95$; and D: $\sigma_1 = 600$, $\sigma_3 = 200$ kPa, $\eta = 1.2$). Then, the stress increment $d\sigma$ in all directions with the same norm ($\|d\sigma\| = 10$ kPa) was imposed, and the corresponding strain response $d\varepsilon$ was computed.

The two sets of parameters for both models in Table 2 were adopted to perform the strain response analysis.

The response envelopes predicted from the two models for the same initial stress states are plotted in Fig. 10. The response envelopes predicted from the two models for initially isotropic stress state (point A) is shown in Fig. 10a. The two response envelopes are almost identical ellipses centered at the origin of the Rendulic plane of strain increments. The predicted response envelopes from point A indicate the response deformations at this stress state are mostly elastic.

Figure 10b–d is the predicted response envelopes from the two models for three anisotropic stress states (i.e., points B, C and D). The patterns of response envelopes for the anisotropic stress states are very different from the

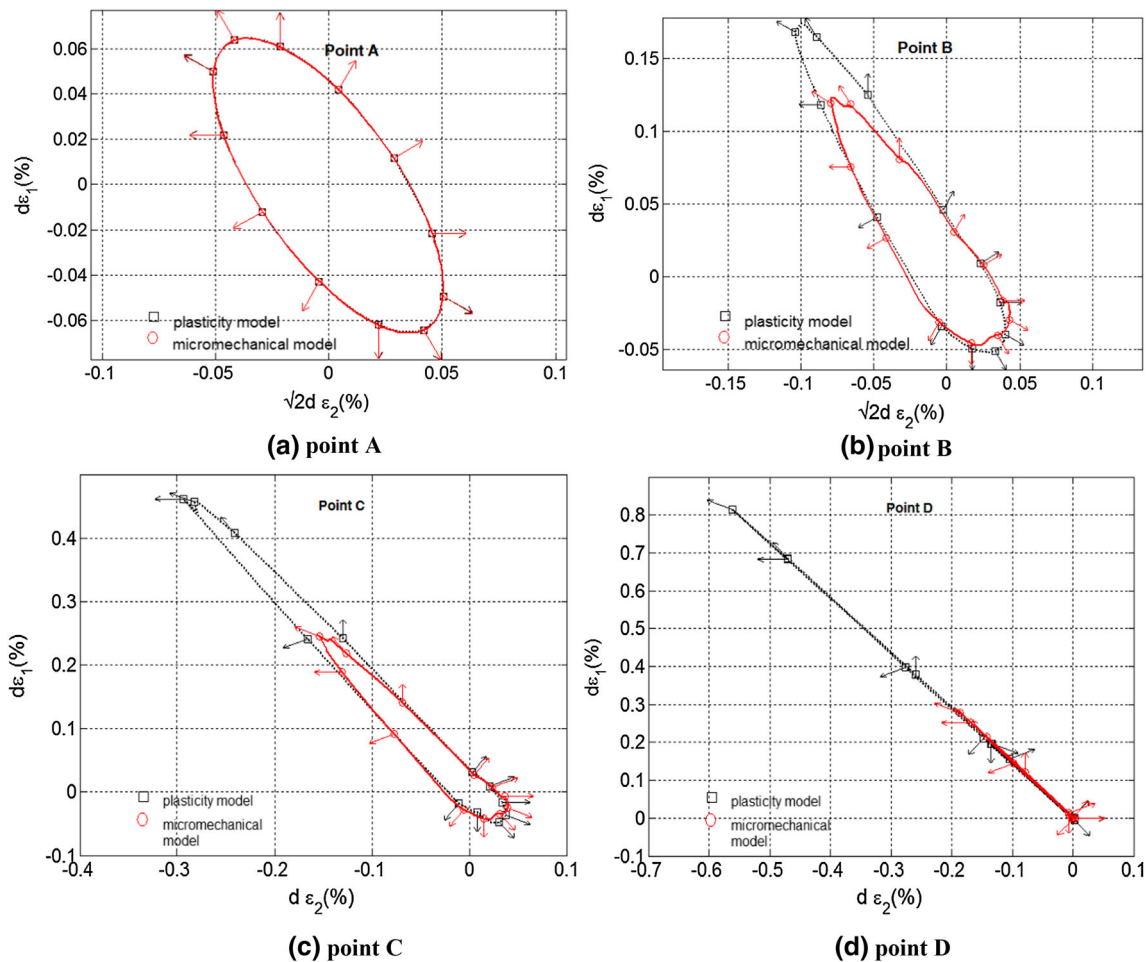


Fig. 10 The predicted strain response envelopes from two models at initially different stress states

ellipsoid response envelopes for the isotropic stress states. The distorted shape of the strain response envelope indicates large plastic strains for some loading directions.

Comparing the strain response envelopes derived from the two models, noteworthy differences are observed, and the amount of differences increases with the applied initial stress ratio. Figure 10 also suggests that the differences of the two models are dependent on the loading directions. For some loading directions, there are not many differences in the predicted results, whereas, for other loading directions, significant differences can be observed.

Figure 10d shows the strain response envelopes for a stress level ($\eta = 1.2$) near critical line (or Coulomb friction line $\eta = 1.234$). According to the discussion by Darve and Nicot [9], near the plastic limit condition, the strain response envelope shrinks into a straight line. This straight line indicates that, at the plastic limiting condition, the direction of the incremental strain vector is independent of the direction of the incremental stress vector.

The dot product of the two tensors, $d\sigma$ and $d\epsilon$ used in the strain response analysis, represents the second-order work,

which is a useful indicator for the instability of the material. It is of interest to check the possible instabilities due to the stress probes in various directions. For convenience, we define a normalized second-order work d^2W_{norm}

$$d^2W_{norm} = \frac{d\sigma d\epsilon}{\|d\sigma\| \|d\epsilon\|} \tag{40}$$

Thus, d^2W_{norm} is equal to the cosine of the angle between $d\sigma$ and $d\epsilon$. Its value is included in the interval of (-1, 1). Figure 11a–d shows rose diagrams showing the variation in d^2W_{norm} with respect to the stress probe direction. In such diagrams, a constant value $c = 1$ is added to the polar value of d^2W_{norm} so that a circle of radius c is drawn in the circular diagrams to represent vanishing values of d^2W_{norm} : inside the circle, d^2W_{norm} is negative; outside the circle, it is positive.

Figure 11 shows the rose diagrams for four different levels of shear stress ($q/p = 0, 0.75, 0.95, 1.2$). The angles shown in Fig. 11 are the stress probing directions (see Fig. 9). Note that the direction of 210 degree is parallel to the hydrostatic axis (reduction of mean stress), and the

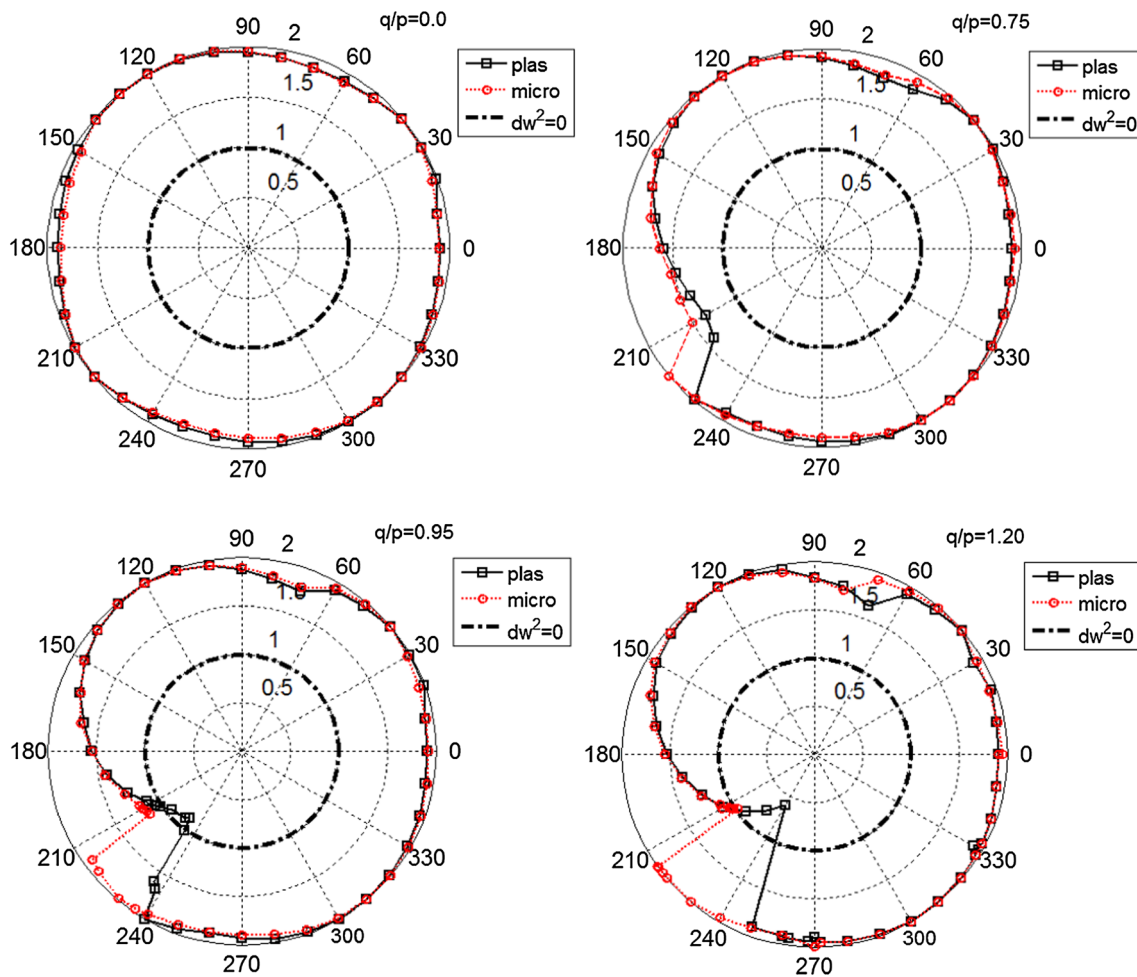


Fig. 11 Results from different models for the same q/p

direction of 240 degree is about parallel to the Coulomb friction line. Figure 11 shows that the instabilities occur for probe directions between these two directions.

The patterns of instability are different for the plasticity model and micromechanical model. For the plasticity model, at $q/p = 0.95$, instabilities already occur for stress probes between 220° and 235° , whereas, for micromechanical model, instabilities do not occur at this stress level. When $q/p = 1.2$, instabilities start to occur in the micromechanical model for stress probe directions in the vicinity of 210° .

6 Summary and conclusions

A conventional plasticity model was constructed by upscaled the micromechanical model by Chang and Hicher [4], and the proposed model belongs to the kind of isotropic hardening model. The mathematically derived relationships between the plasticity model parameters and particle-level properties were presented based on the condition that the

two models would predict the same selected mechanical response, i.e., the isotropic stress condition. A calibration procedure was proposed for both sets of parameters. Then, a comparative study was conducted to investigate the differences of the predicted element behaviors. Some conclusions can be obtained as follows:

(1) To derive the relationship between element-level and contact-level parameters, the constitutive laws (such as yielding condition, dilation pattern and hardening rule, etc.) used in the selected micromechanical model and plasticity model, need to have the same mathematical forms and physical mechanism although they are defined at different scale levels.

(2) For an isotropic hardening plasticity model, the relationship between element-level parameters and contact-level parameters exists only under the isotropic loading condition. Accordingly, parameters of element level and contact level, can be calibrated from the measured mechanical response for a specimen under the isotropic loading condition, for example, the compression response measured from a drained isotropic compression loading

test, and the shear response measured from the beginning of a triaxial load test on an isotropic consolidated sample.

(3) In the micromechanical model, the dependency of the inter-particle behavior with respect to the orientation is modeled. However, the upscaled plasticity model belongs to the type of isotropic hardening model. Thus, different mechanical responses are predicted after the sample becomes anisotropy induced by a deviatoric stress.

The dilatancy developments are very different during shear. For the micromechanical model, the ratio of plastic volumetric strain and shear strain has a nonlinear relationship with stress ratio, whereas, for the conventional plasticity model, the relationship is linear. Besides, the micromechanical model has the ability to predict the stress-induced anisotropy of granular materials and the correspondent change of elastic volumetric strain due to the anisotropy. In the upscaled conventional plasticity model, this mechanism of stress-induced anisotropy cannot be accounted.

(4) Although there are some differences between the two models, it is noted that the upscaled plasticity model is reasonably acceptable for capturing main features of sand behavior in a triaxial loading condition under both drained and undrained situations. However, it can be observed from the strain response envelope analysis that the amount of differences between model predictions are dependent of the loading directions. For loading directions other than triaxial condition, the differences between the upscaled plasticity model and the micromechanical model may be significant.

Acknowledgements Authors appreciate the financial support of Beijing Excellent Talent Training Program (2013D009006000005), National Natural Science Foundation of China (No. 51178044) and National Key Research and Development Program of China (No. 2017YFC0805300).

Appendix 1: Derivation of relationship of parameters of two models

According to Chang and Gao [47], the relationship of k_n^z and B under isotropic compression condition can be expressed as follows,

$$B = \frac{4}{9} \left(\frac{N}{V} \right) r^2 k_n^z \quad (41)$$

where N is contacts number in the representative volume V , and r is the radius of particles.

The relationship of ζ^z and μ can be expressed as follows [26],

$$\zeta^z = \frac{1 - 2\mu}{1 + 3\mu} \quad (42)$$

We consider the problem under drained triaxial compression condition. At the initial point after consolidation with confining pressure σ_c , the effective stress tensor is,

$$\sigma_{ij} = \sigma_c \delta_{ij} \quad (43)$$

In case of isotropic compression, the normal and tangential forces on each plane can be calculated from Eq. (35) in local coordinate (see Fig. 1) as,

$$f_n^z = \sigma_c \frac{3V}{Nl} \quad (44)$$

$$f_s^z = 0 \quad (45)$$

where l is the average branch length between the two particles $l = 2r$.

Given a small total stress increments $d\sigma_{11}$ ($d\sigma_{11} > 0$) in the axial direction, the effective stress increments $\dot{\sigma}_{ij}$ can be written as follows,

$$\dot{\sigma}_{ij} = \begin{bmatrix} d\sigma_{11} & 0 & 0 \\ 0 & 0 & 0 \\ 0 & 0 & 0 \end{bmatrix} \quad (46)$$

The incremental normal force and tangential force on each contact plane can be calculated from Eq. (35) as follows,

$$\begin{aligned} \dot{f}_n^z &= \dot{\sigma}_{11} \frac{3V}{Nl} \cos^2 \theta + \dot{\sigma}_{22} \frac{3V}{Nl} \sin^2 \theta \cos^2 \beta \\ &+ \dot{\sigma}_{33} \frac{3V}{Nl} \sin^2 \theta \sin^2 \beta \end{aligned} \quad (47)$$

$$\begin{aligned} \dot{f}_s^z &= -\dot{\sigma}_{11} \frac{3V}{Nl} \sin \theta \cos \theta + \dot{\sigma}_{22} \frac{3V}{Nl} \sin \theta \cos \theta \cos^2 \beta \\ &+ \dot{\sigma}_{33} \frac{3V}{Nl} \sin \theta \cos \theta \sin^2 \beta \end{aligned} \quad (48)$$

where β, θ are direction angle in Fig. 1.

Substituting Eq. (46) into (47) and (48), the above two equations can be simplified as follows,

$$\dot{f}_n^z = \frac{3V}{Nl} d\sigma_{11} \cos^2 \theta \quad (49)$$

$$\dot{f}_s^z = -d\sigma_{11} \frac{3V}{Nl} \sin \theta \cos \theta \quad (50)$$

We take deviations of hardening equation (Eq. 24) with plastic tangential displacements δ_r^p at the point of $\delta_r^p = 0$; then, we get the incremental plastic tangential displacements $\dot{\delta}_r^p$,

$$\dot{\delta}_r^p = \frac{\dot{f}_s^z}{k_{r0}^p} \quad (51)$$

The incremental plastic normal displacements $\dot{\delta}_n^p$ can be obtained from the dilation equation (Eq. 23),

$$\dot{\delta}_n^p = d \tan \phi_{cs} \dot{\delta}_r^p \quad (52)$$

The global plastic incremental displacements can be obtained as follows,

$$\dot{\delta}_i^p = \dot{\delta}_n^p n_i + \dot{\delta}_r^p s_i \tag{53}$$

The macro-plastic strain increment can be obtained by Eq. (34), which can be written in integration forms as follows,

$$\dot{u}_{j,i}^p = A_{ik}^{-1} l \int_0^{2\pi} \int_0^\pi \dot{\delta}_j^p(\theta, \beta) n_k^z(\theta, \beta) \sin \theta d\theta d\beta \tag{54}$$

Then we get,

$$\begin{aligned} \dot{u}_{1,1}^p &= \frac{2f_n^z d \tan \phi_{cs} d\sigma_{11}}{5 k_{r0}^p l \sigma_c} + \frac{2f_n^z d\sigma_{11}}{5 k_{r0}^p l \sigma_c} \\ \dot{u}_{2,2}^p &= \frac{3 f_n^z d \tan \phi_{cs} d\sigma_{11}}{10 k_{r0}^p l \sigma_c} - \frac{1 f_n^z d\sigma_{11}}{5 k_{r0}^p l \sigma_c} \\ \dot{u}_{3,3}^p &= \dot{u}_{2,2}^p \\ \dot{u}_{1,2}^p &= \dot{u}_{2,1}^p = \dot{u}_{1,3}^p = \dot{u}_{3,1}^p = \dot{u}_{2,3}^p = \dot{u}_{3,2}^p = 0 \end{aligned} \tag{55}$$

So the macro-plastic volumetric strain increment and shear strain increment can be obtained as follows,

$$\dot{\epsilon}_{vol}^p = (\dot{u}_{1,1}^p + \dot{u}_{2,2}^p + \dot{u}_{3,3}^p) = \frac{f_n^z d \tan \phi_{cs} d\sigma_{11}}{k_{r0}^p l \sigma_c} \tag{56}$$

$$\dot{\epsilon}_r^p = \frac{2}{3} (\dot{u}_{1,1}^p - \dot{u}_{3,3}^p) = \frac{2 f_n^z d \tan \phi_{cs} d\sigma_{11}}{30 k_{r0}^p l \sigma_c} + \frac{2 f_n^z d\sigma_{11}}{5 k_{r0}^p l \sigma_c} \tag{57}$$

The plastic strain increment ratio of the micromechanical model can be obtained,

$$\left(\frac{\dot{\epsilon}_{vol}^p}{\dot{\epsilon}_r^p}\right)_0 = \frac{15d \tan \phi_{cs}}{d \tan \phi_{cs} + 6} \tag{58}$$

where the subscript “0” presents the initial state after consolidation.

Substituting Eq. (41) and Eq. (44) into Eq. (56), then we get,

$$\dot{\epsilon}_{vol}^p = \frac{d \tan \phi_{cs}}{3B(k_{r0}^p/k_n^z)} d\sigma_{11} = \frac{d \tan \phi_{cs}}{3B\zeta^p} \dot{q} \tag{59}$$

Substituting Eq. (41) and Eq. (44) into Eq. (57), then we get,

$$\begin{aligned} \dot{\epsilon}_r^p &= \frac{1}{3B\zeta^p} \left(\frac{1}{15} d \tan \phi_{cs} + \frac{2}{5}\right) d\sigma_{11} \\ &= \frac{1}{3B\zeta^p} \left(\frac{1}{15} d \tan \phi_{cs} + \frac{2}{5}\right) \dot{q} \end{aligned} \tag{60}$$

For the conventional plasticity model, at the beginning of shear after consolidation, $q = 0$. The plastic shear strain increment and volumetric strain increment can be obtained from hardening rules and dilating equation as follows,

$$\dot{\epsilon}_r^p = \frac{\dot{q}}{G^p} \tag{61}$$

$$\dot{\epsilon}_{vol}^p = D \left(M - \frac{q}{p}\right) \dot{\epsilon}_r^p = DM \dot{\epsilon}_r^p = DM \frac{\dot{q}}{G^p} \tag{62}$$

So the plastic strain increments ratio of the conventional plasticity model can be obtained,

$$\left(\frac{\dot{\epsilon}_{vol}^p}{\dot{\epsilon}_r^p}\right)_0 = DM \tag{63}$$

Equating (58) and (62), then the relationship of d and D can be obtained as follows,

$$d = \frac{6DM}{\tan \phi_{cs}(15 - DM)} \tag{64}$$

Equating (60) and (61) or Equating (59) and (62), then the relationship of ζ^p and χ can be obtained as follows,

$$\zeta^p = \frac{d \tan \phi_{cs} + 6}{45} \chi \tag{65}$$

where $\zeta^p = \frac{k_n^p}{k_n^z}$, $\chi = \frac{C^p}{B}$.

Under undrained compression conditions, given a small total stress increments $d\sigma_{11}$ ($d\sigma_{11} > 0$) in the axial direction, stress increments $\dot{\sigma}_{ij}$ can be written as,

$$\begin{bmatrix} d\sigma_{11} - du & 0 & 0 \\ 0 & -du & 0 \\ 0 & 0 & -du \end{bmatrix} \tag{66}$$

where du is the water pore pressure increment. Similarly, we can obtain the incremental force on each contact plane from Eq. (35). The incremental plastic displacements $\dot{\delta}_r^p$ and $\dot{\delta}_n^p$ can be calculated by hardening equation (Eq. 24) and the dilation equation (Eq. 23). Then the plastic strain increment can be obtained from Eq. (34). Using the same derivation process, we can obtain the same relationship for parameters of two models, as described by Eqs. (41), (42), (64) and (25), which will not be repeated here.

References

1. Cambou B, Dubujet P, Emeriault F, Sidoroff F (1995) Homogenization for granular materials. Eur J Mech A/Solids 14(2):255–276
2. Chang CS (1988) Micromechanical modeling of constructive relations for granular material. In: Satake M, Jenkins JT (eds) Micromechanics of granular materials. Elsevier, Amsterdam, Oxford, New York, Tokyo, pp 271–279
3. Chang CS, Gao J (1996) Kinematic and static hypotheses for constitutive modeling of granulates considering particle rotation. Acta Mech 115(1–4):213–229

4. Chang CS, Hicher PY (2005) An elasto-plastic model for granular materials with microstructural consideration. *Int J Solids Struct* 42:4258–4277
5. Chang CS, Sundaram SS, Misra A (1989) Initial moduli of particulated mass with frictional contacts. *Int J Numer Anal Methods Geomech* 13(6):629–644
6. Chang CS, Chao SC, Chang Y (1995) Estimates of mechanical properties of Granulates with Anisotropic random packing structure. *Int J Solids Struct* 32(14):1989–2008
7. Christofferson J, Mehrabadi MM, Nemat-Nassar S (1981) A micromechanical description on granular material behavior. *ASME J Appl Mech* 48:339–344
8. Cundall PA, Strack O (1979) A discrete numerical model for granular assemblies. *Geotechnique* 29:47–65
9. Darve F, Nicot F (2005) On flow rule in granular media: phenomenological and multi-scale views (Part II). *Int J Numer Anal Meth Geomech* 29(14):1411–1432
10. Doanh T (2000) Strain response envelope: a complementary tool for evaluating hostun sand in triaxial compression and extension: experimental observations. In: Kolymbas D (ed) *Constitutive modelling of granular materials*. Springer, Berlin, pp 375–396
11. Duncan JM, Chang CY (1970) Nonlinear analysis of stress and strain in soils. *Proc ASCE JSMFD* 96(5):1629–1633
12. Gudehus G (1979) A comparison of some constitutive laws for soils under radially symmetric loading and unloading. In: Wittke W (ed) *Proceedings of 3rd international conference on numerical methods in geomechanics*, Balkema, pp 1309–1323
13. Hicher P-Y, Chang CS (2006) Anisotropic non linear elastic model for particulate materials. *J Geotech Environ Eng ASCE* 132(8):1052–1061
14. Hu N, Yu HS, Yang DS, Zhuang PZ (2019) Constitutive modelling of granular materials using a contact normal-based fabric tensor. *Acta Geotech*. <https://doi.org/10.1007/s11440-019-00811-z>
15. Irani N, Remmers JJC, Deshpande VS (2015) Finite strain discrete dislocation plasticity in a total Lagrangian Setting. *J Mech Phys Solids* 83:160–178
16. Ishihara K, Tatsuoka F, Yasuda S (1975) Undrained deformation and liquefaction of sand under cyclic stresses. *Soils Found* 15(1):29–44
17. Jefferies MG (1993) Nor-Sand: a simple critical state model for sand. *Geotechnique* 43(1):91–103
18. Jenkins JT (1988) Volume change in small strain axisymmetric deformations of a granular material. In: Satake M, Jenkins JT (eds) *Micromechanics of granular materials*. Elsevier, Amsterdam, Oxford, New York, Tokyo, pp 143–152
19. Jenkins JT, Strack ODL (1993) Mean-field inelastic behavior of random arrays of identical spheres. *Mech Mater* 16:25–33
20. Kolymbas D (2000) Response-envelopes: a useful tool as “hypoplasticity then and now”. In: Kolymbas D (ed) *Constitutive modelling of granular materials*. Springer, Berlin, pp 57–105
21. Konishi Y, Hyodo M, Ito S (2007) Compression and undrained shear characteristics of sand-fines mixtures with various plasticity. *JSCE J Geotech Eng Geoenviron Eng* 63(4):1142–1152 (in Japanese)
22. Krut NP (2014) Micromechanical study of elastic moduli of three-dimensional granular Assemblies. *Int J Solids Struct* 51:2336–2344
23. Krut NP, Rothenburg L (2002) Micromechanical bounds for the effective elastic moduli of granular materials. *Int J Solids Struct* 39(2):311–324
24. Lade PV, Duncan JM (1977) Elasto-plastic stress-strain theory for cohesionless soils with curved yield surface. *Int J Solids Struct* 13(11):1019–1035
25. Lewin P, Burland J (1970) Stress-probe experiments on saturated normally consolidated clay. *Geotechnique* 20(1):38–56
26. Liao CL, Chan TC, Suiker ASJ, Chang CS (2000) Pressure-dependent elastic moduli of granular assemblies. *Int J Anal Numer Methods Geomech* 24:265–279
27. Luong, M.P., 1980. Stress-strain aspects of cohesionless soils under cyclic and transient loading. In: *International symposium on soils under cyclic and transient loading*, Swansea, pp 353–376
28. Maleej Y, Dormieux L, Sanahuja J (2009) Micromechanical approach to the failure criterion of granular media. *Eur J Mech A/Solids* 28:647–653
29. Manzari MT, Dafalias YF (1997) A critical state two-surface plasticity model for sands. *Geotechnique* 47(2):255–272
30. Matsuoka H, Takeda K (1980) A stress-strain relationship for granular materials derived from microscopic shear mechanisms. *Soils Found* 20(3):45–58
31. Misra A, Poursolhjouy P (2016) Elastic behavior of 2D grain packing modeled as micromorphic media based on granular micromechanics. *J Eng Mech* 143(1):C4016005
32. Misra A, Poursolhjouy P (2017) Grain- and macro-scale kinematics for granular micromechanics based small deformation micromorphic continuum model. *Mech Res Commun* 81:1–6
33. Misra A, Singh V (2014) Nonlinear granular micromechanics model for multi-axial rate-dependent behavior. *Int J Solids Struct* 51(13):2272–2282
34. Misra A, Yang Y (2010) Micromechanical model for cohesive materials based upon pseudo-granular structure. *Int J Solids Struct* 47:2970–2981
35. Ng TT, Petrakis E (1996) Small-strain response of random arrays of spheres using discrete element method. *J Eng Mech* 122(3):239–244
36. Nicot F, Darve F (2007) Basic features of plastic strains: from micro-mechanics to incrementally nonlinear models. *Int J Plast* 23:1555–1588
37. Nicot F, Darve F (2011) The H-microdirectional model: accounting for a mesoscopic scale. *Mech Mater* 43:918–929
38. Nicot F, Sibille L, Darve F (2012) Failure in rate-independent granular materials as a bifurcation toward a dynamic regime. *Int J Plast* 29(1):136–154
39. Papadimitriou AG, Chaloulos YK, Dafalias YF (2019) A fabric-based sand plasticity model with reversal surfaces within anisotropic critical state theory. *Acta Geotech* 14:253–277
40. Rothenburg L, Selvadurai APS (1981) Micromechanical definitions of the Cauchy stress tensor for particular media. In: Selvadurai APS (ed) *Mechanics of structured media*. Elsevier, Amsterdam, pp 469–486
41. Sibille L (2011) Directional stress probes to exhibit constitutive behavior of discrete element models. In: *Olek Zienkiewicz Course 2011—Discrete Mechanics of Geomaterials*, Grenoble, June 27th–July 1st
42. Steinhauser MO, Grass K, Strassburger E, Blumen A (2009) Impact failure of granular materials—Non-equilibrium multiscale simulations and high-speed experiments. *Int J Plast* 25(1):161–182
43. Tamagnini C, Mašin D, Costanzo D, Viggiani G (2006) An evaluation of different constitutive models to predict the directional response of a reconstituted fine-grained soil. In: Wu W, Yu HS (eds) *Modern trends in geomechanics*, vol 106. Springer, Berlin, pp 143–157
44. Tran T-H, Monchiet V, Bonnet G (2012) A micromechanics-based approach for derivation of constitutive elastic coefficients of strain-gradient media. *Int J Solids Struct* 49(5):783–792
45. Walton K (1987) The effective elastic moduli of a random packing of spheres. *J Mech Phys Solids* 35:213–226
46. Wood D (1990) *Soil behavior and critical state soil mechanics*. Cambridge University Press, Cambridge
47. Wood D, Belkheir K, Liu D (1994) Strain softening and state parameter for sand modelling. *Geotechnique* 44(2):335–339

48. Xiong H, Nicot F, Yin ZY (2017) A three-dimensional micromechanically based model. *J Numer Anal Methods Geomech, Int.* <https://doi.org/10.1002/nag.2692>
49. Yin ZY, Chang CS, Hicher PY, Karstunen M (2009) Micromechanical Analysis of Kinematic Hardening in Natural Clay. *Int J Plast* 25(8):1413–1435
50. Zhu QZ, Shao JF, Mainguy M (2010) A micromechanics-based elastoplastic damage model for granular materials at low confining pressure. *Int J Plast* 26:586–602

Publisher's Note Springer Nature remains neutral with regard to jurisdictional claims in published maps and institutional affiliations.